*Article*

# The Echo Method for Axion Dark Matter Detection

Ariel Arza [1],*,[†] and Elisa Todarello [2,3,4],*,[†]

1   Institute for Theoretical and Mathematical Physics, Lomonosov Moscow State University (ITMP), 119991 Moscow, Russia
2   Institut für Astroteilchenphysik, Karlsruhe Institute of Technology (KIT), Hermann-von-Helmholtz-Platz 1, 76344 Eggenstein-Leopoldshafen, Germany
3   Dipartimento di Fisica, Università di Torino, Via P. Giuria 1, 10125 Torino, Italy
4   Istituto Nazionale di Fisica Nucleare, Sezione di Torino, Via P. Giuria 1, 10125 Torino, Italy
*   Correspondence: aarza@itmp.msu.ru (A.A.); todarello@phys.ufl.edu (E.T.)
†   These authors contributed equally to this work.

**Abstract:** The axion is a dark matter candidate arising from the spontaneous breaking of the Peccei–Quinn symmetry, introduced to solve the strong CP problem. It has been shown that radio/microwave radiation sent out to space is backscattered in the presence of axion dark matter due to stimulated axion decay. This backscattering is a feeble and narrow echo signal centered at an angular frequency very close to one-half of the axion mass. In this article, we summarize all the relevant results found so far, including analytical formulas for the echo signal, as well as sensitivity prospects for possible near-future experiments.

**Keywords:** axions; dark matter; axion detection

## 1. Introduction

The nature of dark matter is one of the most intriguing puzzles of modern science. The lack of signals from thermally produced WIMP dark matter suggests the exploration of new routes. One possibility is hypothetical particles produced in the early universe by nonthermal means. Such is the case for sterile neutrinos [1], dark photons [2], and QCD axions [3–5] (or axion-like particles (ALPs) [6]), which have became very popular in the last few years.

The QCD axion is a hypothetical particle that was originally postulated as a solution to the strong CP problem of the Standard Model of particle physics, i.e., the puzzle of why the strong interactions conserve the P and CP symmetries [3]. The QCD axion and ALPs are leading dark matter candidates in the sub-eV mass range [7–10]. Their nonthermal production mechanisms include the realignment and decay of topological defects.

Several running experiments are carrying out the search for axions, and there are also many new interesting proposed ideas. See [11,12] for recent reviews. Most of these detection schemes are based on the axion to two-photon coupling [13].

Thanks to this coupling, a massive axion is allowed to decay spontaneously into two photons, and more interestingly, the decay rate is enhanced considerably in a photon background with photon energy close to half the axion mass. This stimulated axion decay has been discussed extensively in the recent literature [14–20]. In the axion rest frame, the photons ejected from the axion decay are forced to propagate along the trajectory of the incident photon. While one of the decaying photons is released together with the incident one, the other must be released exactly in the opposite direction due to the conservation of momentum. Reference [21] discussed the possibility of sending out to space a powerful beam of microwave (or radio) electromagnetic radiation as an axion decay stimulator and then "listening" for the incoming radiation, the echo. The power signal of the echo was estimated, giving promising results for radio astronomy searches. The atmosphere's transparency mainly constrains the frequency range for which the echo method is realistic.

At sea level, this corresponds approximately to the range 30 MHz–30 GHz, equivalent to axion masses between $2.5 \times 10^{-7}$ eV and $2.5 \times 10^{-4}$ eV. Of course, this is just to have an idea. At a certain altitude, the method could be extended even to infrared or visible light, depending on the telescope's frequency operation, location, weather, noise temperature, etc. A more detailed and exhaustive analysis of the echo signal can be found in [22].

The echo intensity has three relevant properties: (1) it depends strongly on the local axion dark matter momentum distribution; (2) it does not depend on the shape of the outgoing beam; (3) its frequency is shifted with respect to the outgoing beam's frequency by the axion's average momentum in the beam direction.

In this article, we provide a summary of the results found in [21,22]. In Section 2, we calculate, in a simple manner, the total power of the echo wave, while in Section 3, we specify how this power is spatially distributed. In Section 4, we discuss the sensitivity prospects of the method based on realistic radio astronomy equipment, and finally, in Section 5, we conclude.

## 2. Power in the Echo Wave

The first step of our discussion is to compute the power stored in the echo wave. Let $\vec{A}^{(0)}(\vec{x}, t)$ be the outgoing beam vector potential and $a(\vec{x}, t)$ the ambient dark matter axion field. The interaction of the outgoing beam with the axion field results in a perturbative correction $\vec{A}^{(1)}(\vec{x}, t)$ to the zero-order $\vec{A}^{(0)}(\vec{x}, t)$. In the Coulomb gauge, this correction satisfies the inhomogeneous wave equation:

$$\left(\partial_t^2 - \nabla^2\right)\vec{A}^{(1)} = -g\partial_t a\vec{\nabla} \times \vec{A}^{(0)}. \tag{1}$$

We also neglected terms containing gradients of $a$. This is justified by the assumption of a nonrelativistic axion background. From now on, we will always ignore this kind of contribution.

For the time being, let us just consider one axion's momentum mode with energy density $\rho(\vec{p})$. The axion field can be written as:

$$a_p(t, \vec{x}) = \frac{\sqrt{2\rho(\vec{p})}}{E_p}\sin(E_p t - \vec{p} \cdot \vec{x}), \tag{2}$$

where $E_p = \sqrt{m^2 + p^2}$. As $E_p = m + \mathcal{O}(p^2)$, we use $E_p \approx m$ throughout this article.

Let us expand the source field $\vec{A}^{(0)}$, as well as the correction $\vec{A}^{(1)}$ in Fourier modes as:

$$\vec{A}^{(0)}(t, \vec{x}) = \int \frac{d^3k}{(2\pi)^3} \, \hat{e} \, \mathcal{A}_0(\vec{k}) \, e^{-i(\omega(k)t - \vec{k}\cdot\vec{x})} \tag{3}$$

$$\vec{A}^{(1)}(t, \vec{x}) = \int \frac{d^3k}{(2\pi)^3} \, \hat{k} \times \hat{e} \, A^{(1)}(t, \vec{k}) \, e^{i\vec{k}\cdot\vec{x}}. \tag{4}$$

Here, we assumed an incident field polarized in the direction $\hat{e}$. $A^{(1)}$ is polarized necessarily in the direction $\hat{k} \times \hat{e}$, except for small corrections of the order of $p$. We also defined $\omega(k) \equiv |\vec{k}|$. Keeping only terms relevant to the stimulated axion decay, i.e., the photon momentum modes $\vec{k}$ and $\vec{q} = \vec{p} - \vec{k}$, Equation (1) becomes:

$$\left(\partial_t^2 + \omega(q)^2\right)A^{(1)}(t, \vec{q}) = -ig\sqrt{\frac{\rho(\vec{p})}{2}}\,\omega(k)\,\mathcal{A}_0(\vec{k})^* e^{-i(m - \omega(k))t}. \tag{5}$$

By looking at the source term of the above equation, we see that when $m > \omega(k)$, the solution describes a wave that travels backwards with respect to the incident one. We call it the echo wave. The echo wave is excited when $\omega(q)$ is equal or very close to $m - \omega(k)$, i.e., when $\omega(k) \approx m/2$. Now, we look for a resonant solution using the ansatz

$A^{(1)}(t,\vec{q}\,) = \mathcal{A}(t,\vec{q}\,)e^{-i\omega(q)\,t}$ where $\mathcal{A}(t,\vec{q}\,)$ varies slowly in time with respect to $A^{(1)}(t,\vec{q}\,)$. Neglecting the second derivatives of $\mathcal{A}(t,\vec{q}\,)$ in Equation (5), we obtain the solution:

$$\mathcal{A}(t,\vec{q}\,) = \frac{g}{2}\sqrt{\frac{\rho(\vec{p}\,)}{2}}\,\mathcal{A}_0(\vec{k}\,)^*\,e^{i\,\epsilon(\vec{k},\vec{p}\,)\,t}\left(\frac{\sin(\epsilon(\vec{k},\vec{p}\,)\,t/2)}{\epsilon(\vec{k},\vec{p}\,)/2}\right), \tag{6}$$

where $\epsilon(\vec{k},\vec{p}\,) = \omega(k) + \omega(|\vec{p}-\vec{k}|) - m$. In the limit $\epsilon t \gg 1$, we can substitute $\sin(\epsilon t/2)/\epsilon \to \pi\delta(\epsilon)$ in Equation (6). Integrating over all axion's momentum modes and assuming that the incident beam propagates mostly in a preferred direction (the direction of $\vec{k}$ is fixed), the echo power is found to be:

$$P = \frac{\pi}{4}\,g^2\,t_{\text{off}}\int dp_\parallel\,\frac{\partial\rho}{\partial p_\parallel}\int d\omega\,\frac{\partial P_0}{\partial\omega}\,\delta(\epsilon(\omega,p_\parallel)), \tag{7}$$

where $\vec{p}_\parallel$ is the axion's momentum projected in the direction of $\vec{k}$. To obtain this result, we assumed that the energy is provided by a source emitting a constant power $P_0$ from $t=0$ until $t=t_{\text{off}}$.

Let us perform the integral (7) in two scenarios: when the bandwidth of the beam $\delta\omega$ is much bigger than the momentum bandwidth of the axion $\delta p$ and in the opposite case. For $\delta\omega \gg \delta p$, the axion distribution can be considered as if it were condensed at a single value $\bar{p}_\parallel$. We then approximate $\partial\rho/\partial p_\parallel = \rho\,\delta(p_\parallel - \bar{p}_\parallel)$. We straightforwardly find:

$$P = \frac{\pi}{8}g^2\rho\,\frac{\partial P_0}{\partial\omega_*}\,t_{\text{off}}, \tag{8}$$

where:

$$\omega_* = \frac{m + \bar{p}_\parallel}{2}. \tag{9}$$

For $\delta\omega \ll \delta p$, we have $\partial P_0/\partial\omega = P_0\,\delta(\omega - \bar{\omega})$. We find:

$$P = \frac{\pi}{4}g^2\,P_0\,\frac{\partial\rho}{\partial p_{\parallel\,*}}\,t_{\text{off}}, \tag{10}$$

where:

$$p_{\parallel\,*} = 2\bar{\omega} - m. \tag{11}$$

For the DFSZ model of the QCD axion, an input power of $1\,\text{kW}$ over a bandwidth of $1\,\text{kHz}$ working for one hour provides a total echo power of $P \sim 10^{-19}\,\text{W}\left(\frac{m}{10^{-4}\,\text{eV}}\right)^2$, which is in principle not too difficult to detect with current radio astronomy technology. Unfortunately, as discussed in [21], due to the nontrivial axion's velocity distribution, this power spreads over a surface that eventually exceeds the detector's size. This effect is easy to visualize if we consider what happens for a single axion decay. If the decaying axion moves with a velocity not perfectly aligned with the incident photon (outgoing beam), the echo photon is released in a direction also different from the incident photon's trajectory. In fact, if the echo photon has energy $\Omega$, the conservation of momentum implies $\Omega\sin(\chi) = mv_\perp$, where $\chi$ is the angle formed by the trajectories of both photons and $v_\perp$ is the component of the axion's velocity perpendicular to the incident photon momentum. From energy conservation, $\Omega$ is equal to $m/2$ plus small corrections; therefore, $\sin(\chi) \simeq 2v_\perp$. As the axion's velocities are of the order of $10^{-3}$ or smaller, we can write $\chi \simeq 2v_\perp$. It follows that, for instance assuming the isothermal sphere model [23] for the galactic halo, which has a velocity dispersion of $270\,\text{km/s}$, the echo spreads over approximately $10^6\,\text{km}$ after 1 h. Even in the caustic ring model of the galactic halo [24], where the minimal axion transverse velocity we can achieve is about $5\,\text{km/s}$, the spread is at least $10^4\,\text{km}$ after the same amount of time. The echo power signal is thus strongly

dependent on the model for the axion phase-space distribution, as well as the size of the detection apparatus. The following section is devoted to analyzing these effects by computing the echo intensity as a function of the spacetime coordinates.

## 3. Echo Intensity

The total power in the echo wave, computed in the previous section, does not carry any information about how it is spatially distributed. As explained above, this spatial dependence is closely related to the axion's velocity distribution, and it especially depends strongly on the transverse components of the axion's velocity. This section is dedicated to characterizing these effects by computing the echo intensity as a function of the spacetime coordinates.

### 3.1. Echo of a Dish Antenna Beam

To develop a sense of how the transverse axion's velocities affect the signal, we perform a simple and useful computation of the echo intensity for some particular models of the axion's velocity distribution. Moreover, as an incident wave, we take the beam emitted by a parabolic dish antenna. Although the parabolic antenna case is the most realistic setup we can address in this work, our findings are limited by scenarios where analytical approximations are possible. These approximations will be explained throughout the text.

Given the axion field $a(t, \vec{x})$ and outgoing beam magnetic field $\vec{B}^{(0)}(t, \vec{x})$, the echo vector potential field $\vec{A}^{(1)}(t, \vec{x})$ is determined by:

$$\vec{A}^{(1)}(t, \vec{x}) = -g \int d^3x' \int dt' \, \frac{\delta(t - t' - |\vec{x} - \vec{x}'|)}{4\pi|\vec{x} - \vec{x}'|} \, \partial_{t'} a(t', \vec{x}') \vec{B}^{(0)}(t', \vec{x}'). \tag{12}$$

We write the axion dark matter field, in a large volume $V$, as an expansion in momentum modes as:

$$a(t, \vec{x}) = \frac{a_0}{2} e^{-imt} \sqrt{\frac{V}{(2\pi)^3}} \int d^3p \, f_a(\vec{p}) \, e^{i(\vec{p} \cdot \vec{x} + \phi_{\vec{p}})} + c.c. \tag{13}$$

where $\vec{p}$ is the axion's momentum in the experiment's rest frame and $\phi_{\vec{p}}$ random phases. These phases are not known and are usually modeled as uniformly distributed random numbers [25–27]. In this article, we limit ourselves to considering the ensemble average:

$$\left\langle e^{-i(\phi_{\vec{p}} - \phi_{\vec{p}'})} \right\rangle_{\text{ens}} = \frac{(2\pi)^3}{V} \delta^3(\vec{p} - \vec{p}'). \tag{14}$$

We leave a discussion of the statistics of the signal to future work. We normalize $f_a(\vec{p})$ as:

$$\int d^3p \, |f_a(\vec{p})|^2 = 1. \tag{15}$$

We considered a parabolic antenna of radius $R$ fed by a plane wave with electric field amplitude $E_0(\omega)$, $\omega$ being the wave's frequency. The electric field emitted by the antenna is known analytically in the far-field zone, i.e., for distances of order $\omega R^2$ or larger from the emission spot. Assuming that the center of the antenna is located at $\vec{x} = 0$ and that the central component of the beam propagates along $\hat{z}$, the antenna's electric field can be written in spherical coordinates as:

$$\vec{E}^{(0)}(t, \vec{x}, \omega) = \hat{x} \, i \frac{E_0(\omega)}{2} \omega R^2 \frac{J_1(\omega R \sin(\theta))}{\omega R \sin(\theta)} \frac{e^{-i\omega(t-r)}}{r}, \tag{16}$$

where $J_1(x)$ is the Bessel function of the first kind of order one. For Equation (16) to be a good approximation, we need most of the echo to be produced in the far-field zone.

Therefore, for an outgoing beam turned on at $t = 0$, our approximation is valid for $t \gg \omega R^2$.

We perform the integral (12) in the limit $\omega R \gg 1$, which is valid for any experimental setup we consider in this article. If the outgoing beam is emitted continuously from $t = 0$, the maximum echo spectral intensity at the emission spot is:

$$\frac{\partial I(t)}{\partial \Omega_*} = \frac{1}{8} \sqrt{\frac{\pi}{2}} \frac{g^2 \rho}{\delta p_z} \min\left(t, R\left\langle v_\perp^{-1} \right\rangle\right) \frac{dI_0}{d\omega_*}, \tag{17}$$

where $\vec{v}_\perp = \vec{p}_\perp / m$ is the axion's transverse velocity and $\Omega_* = (m - \langle p_z \rangle)/2$. The symbol $\langle \rangle$ means averaging over the axion's velocity distribution $|f_a(\vec{v})|^2$.

We can see from the above result that the echo signal depends strongly on the local axion's velocity distribution. Indeed, it scales as the inverse of the momentum dispersion in the forward direction and the inverse of the average transverse velocity component. This paper considered two models for the velocity distribution in the Milky Way, the isothermal sphere and the caustic ring model. In the isothermal model, $|f_a(\vec{v})|^2$ has a Maxwell–Boltzmann behavior with dispersion $\delta v = 270 \, \text{km/s}$ and the average velocity given by the velocity of the Sun in the galactic rest frame, i.e., $|\langle \vec{v} \rangle| \simeq 230 \, \text{km/s}$. In the caustic ring model, the local dark matter is dominated by a single (or a few) cold flow with velocity dispersion $\delta v < 70 \, \text{m/s}$ and with an average velocity of $|\langle \vec{v} \rangle| \simeq 290 \, \text{km/s}$ relative to us. For the isothermal model, we have that $\left\langle v_\perp^{-1} \right\rangle^{-1} = \sqrt{2\pi/3}\,\delta v$ if the outgoing beam points mainly towards the direction of the axion wind. For the caustic ring model, $\left\langle v_\perp^{-1} \right\rangle$ does not depend on its very small dispersion, but it only depends on the direction of the big flow. The direction of the big flow is determined by the position of the IRAS [28], Planck [29] and GAIA [30] triangles with an uncertainty of 0.01 rad. This implies that $\left\langle v_\perp^{-1} \right\rangle^{-1}$ cannot be reduced to values smaller than $5 \, \text{km/s}$.

In this analysis, we saw how the axion's velocity distribution influences the echo signal. Equation (17) shows the effects explicitly. For $t < R\left\langle v_\perp^{-1} \right\rangle$, the echo has not yet spread beyond the emission region, leading to the linear growth of the intensity, in agreement with the results of Section 2. After $t = R\left\langle v_\perp^{-1} \right\rangle$, the intensity saturates suddenly to a constant value, due to the transverse velocity effects. This abrupt change in the intensity behavior is a consequence of the approximations employed, the assumption that most of the echo is coming from the far-field zone. If we had also taken into account the near behavior of the outgoing beam, the transition to the saturated regime would have been smooth. Another limitation of our result is that Equation (17) gives us an approximated value for locations nearby the emission spot. A complete characterization of the outgoing beam would allow us to know the local values of the intensity in more detail. Unfortunately, there is no simple analytical expression for the antenna's emitted field in the near zone. Nevertheless, this issue is addressed in Section 3.2 by constructing a simple and well-behaved model of the outgoing beam in the near zone.

### 3.2. Paraxial Gaussian Beam

To gain further insights into the intensity as a function of the position and into the transition to the saturated regime, we take a simplified model for the outgoing beam. This beam features a simple shape in the near-field zone and matches the antenna beam's far-field zone behavior correctly. Given this beam, we use the paraxial approximation to obtain the local values of the echo intensity as well as its time evolution. We write the beam magnetic field as a transverse wave propagating in the $z$ direction with small transverse corrections:

$$\vec{B}^{(0)}(t, \vec{x}, \omega) = \hat{\epsilon} \, \frac{B_0(\omega)}{2} \, \eta(\vec{x}, \omega) \, e^{-i\omega(t-z)}. \tag{18}$$

For the spatial shape of the beam $\eta(\vec{x}, \omega)$, we take the paraxial Gaussian beam used in laser physics:

$$\eta(\omega, \vec{x}) = \frac{R}{w(z)} e^{-\frac{r^2}{2w(z)^2}} e^{i\omega \frac{r^2}{2\mathcal{R}(z)}}, \tag{19}$$

where $(r, \phi, z)$ are cylindrical coordinates. Here, $w(z)$ is the effective radius of the beam and $\mathcal{R}(z)$ is the radius of curvature of the wavefronts. Their mathematical expressions are:

$$w(z) = R\sqrt{1 + \frac{z^2}{z_R^2}}, \qquad\qquad \mathcal{R}(z) = \frac{z^2 + z_R^2}{z},$$

where $R = w(0)$ and $z_R = \omega R^2$.

The beam is turned on at $t = 0$. At a time $t > 0$, it extends from $z = 0$ to $z = t$. After the beam is turned off at $t = t_{\text{off}}$, it extends from $z = t - t_{\text{off}}$ to $z = t$.

We describe the local dark matter axion field as a superposition of plane waves, in the same way as in Section 3.1 (see Equations (13)–(15)). In addition, we also assumed that $f_a(\vec{p})$ can be factorized in its forward and transverse parts. In the limit $\delta p_z t \gg 1$, after averaging over random phases, the spectral echo intensity at resonance can be written as:

$$\frac{\partial I(t, \vec{x}_\perp)}{\partial \Omega_*} = \frac{1}{8} \sqrt{\frac{\pi}{2}} \frac{g^2 \rho}{\delta p_z} \mathcal{T}(t, \vec{x}_\perp) \frac{dI_0}{d\omega_*}, \tag{20}$$

where the quantity $\mathcal{T}(t, \vec{x}_\perp)$ has units of time and contains all the three-dimensional effects. In a one-dimensional treatment, we have simply $\mathcal{T}(t, \vec{x}_\perp) = \min(t, t_{\text{off}})$ (see [22]), while in three dimensions, the behavior is more complicated. The lateral spread leads to the saturation of the intensity on a characteristic time scale, which is given below. On the other hand, we find null effects coming from the outgoing beam divergence.

We first considered the case of a negligible axion velocity dispersion. In this case, all axions move with approximately the same velocity. We denote the axion's velocity in the plane perpendicular to the beam direction of propagation as $\vec{v}_p$. We analyzed the small velocity dispersion case in two scenarios: (a) $t_{\text{off}} < R/v_p$ and (b) $t_{\text{off}} > R/v_p$.

In Scenario (a), for $t < t_{\text{off}}$, $\mathcal{T}(t, \vec{x}_\perp)$ grows linearly in time, featuring a transverse Gaussian profile with effective radius $R$. For $t > t_{\text{off}}$, i.e., after the outgoing beam is turned off, the Gaussian keeps the maximum value reached at $t = t_{\text{off}}$ and moves rigidly with velocity $\vec{v}_p$. In Scenario (b), for $t < R/v_p$, the intensity grows linearly in time with a Gaussian profile, just as in Scenario (a) before $t_{\text{off}}$. Later, for $R/v_p < t < t_{\text{off}}$, the echo spreads along the direction of $\vec{v}_p$ at a speed $v_p$, forming a "sausage"-shaped profile (see Figure 1). The energy that in Scenario (a) accumulates at the emission spot now spreads laterally, making the echo intensity saturate at any coordinate $\vec{x}_\perp$ when $t > \frac{r\cos(\phi)}{v_p}$, $\phi$ being the angle between $\vec{x}_\perp$ and $\vec{v}_p$. The maximum saturated value is reached at locations where $\phi = 0$ and $R < r\cos(\phi) < v_p t$. The corresponding value for $\mathcal{T}$ within this region is:

$$t_a \approx \frac{R}{v_p}. \tag{21}$$

Finally, for $t > t_{\text{off}}$, the "sausage" moves rigidly at speed $\vec{v}_p$, keeping a fixed length $v_p t_{\text{off}}$ and a width $2R$.
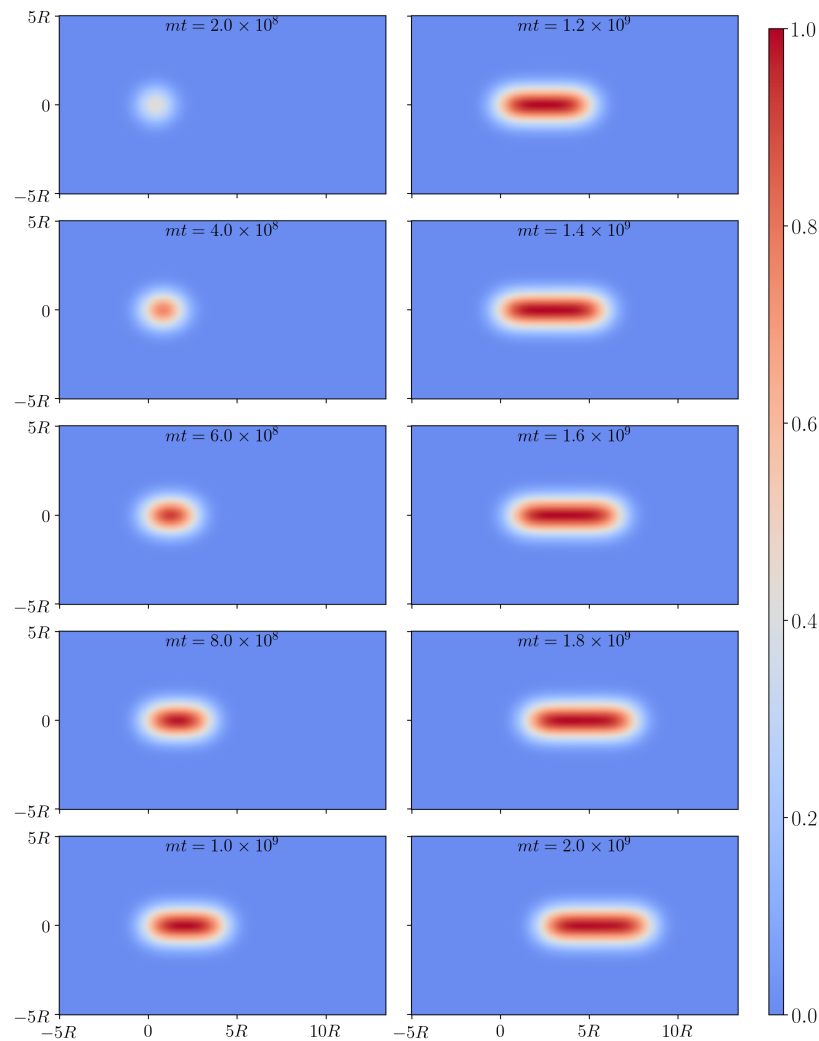
**Figure 1.** Echo intensity form factor $F(t, \vec{x}_\perp)$ at resonance $\omega = \omega_*$ in the case of saturation due to the transverse average axion's velocity. The beam is turned on at $t = 0$ and turned off at $mt_{\text{off}} = 1.4 \times 10^9$. The radius of the emitter is set to $mR = 4000$. The axion's velocity components are those of the caustic ring model, with minimum transverse velocity $v_x = 5$ km/s and $v_z = 290$ km/s. The velocity dispersion is 70 km/s in the $z$ direction. The saturation time is $mt_{\text{sat}} \approx mt_a = 4.3 \times 10^8$.

Next, we considered the case in which the axion transverse velocity dispersion $\delta v_\perp$ dominates over the transverse average velocity. Again, we divided our discussion into scenarios: (a) $t_{\text{off}} < R/\delta v_\perp$ and (b) $t_{\text{off}} > R/\delta v_\perp$. In Scenario (a), the intensity grows at first linearly in time, keeping a Gaussian shape, as in the small velocity dispersion case. After $t_{\text{off}}$, the maximum intensity stays constant at the value obtained at $t = t_{\text{off}}$, and the Gaussian shape stays unchanged. Finally, for times larger than $R/\delta v_\perp$, the value of the intensity decreases as $(\delta v_\perp t)^{-2}$ and the radial extension becomes $\delta v_\perp t$, i.e., the energy spreads radially at velocity $\delta v_\perp$. In Scenario (b), we have again the Gaussian profile with a linearly growing maximum value for $t < R/\delta v_\perp$. For $R/\delta v_\perp < t < t_{\text{off}}$, the energy spreads radially, making the intensity saturate for all the positions satisfying $r < \delta v_\perp t$ (see Figure 2). The maximum value of $\mathcal{T}$ in this saturated regime is found at $r = 0$ and is:

$$t_b \approx \frac{R}{\delta v_\perp}. \tag{22}$$

After $t_{\text{off}}$, the intensity falls off as $(\delta v_\perp t)^{-2}$.

The characteristic times $t_a$ and $t_b$ are not only the saturated values of $\mathcal{T}$ in the respective scenarios, but also the timescales over which the saturation is achieved. We can then define the saturation time:

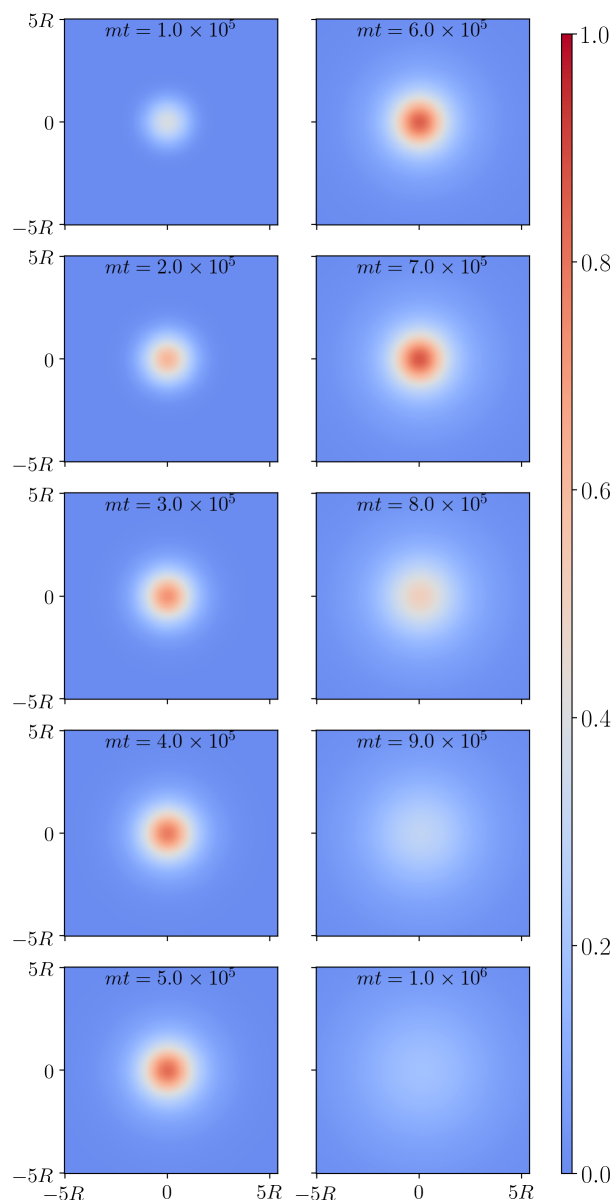$$t_{\text{sat}} = \left( \frac{1}{t_a^2} + \frac{1}{t_b^2} \right)^{-1/2}.$$
(23)



**Figure 2.** Echo intensity form factor $F(t, \vec{x}_\perp)$ at resonance $\omega = \omega_*$ in the case of saturation due to velocity dispersion effects. The beam is turned on at $t = 0$ and turned off at $mt_{\text{off}} = 7 \times 10^5$. The radius of the emitter is set to $mR = 100$. The axion's velocity components are those of the isothermal model, with $v_x = 10$ km/s and $v_z = 230$ km/s, while the velocity dispersion is $270/\sqrt{3}$ km/s in each direction. The saturation time is $mt_{\text{sat}} \approx mt_b = 2.1 \times 10^5$.

To confirm the results of the discussion above, we solve Equation (1) numerically in the paraxial limit, with the model beam Equations (18) and (19). We plot the intensity in the $z = 0$ plane for the caustic ring model and the isothermal sphere, corresponding to the small dispersion and large dispersion cases discussed above, respectively.

We write the echo intensity as:

$$\frac{dI(t,\vec{x}_\perp)}{d\Omega} = \frac{1}{8}\sqrt{\frac{\pi}{2}}\frac{g^2\rho}{\delta p_z}\,t_{\text{sat}}F(t,\vec{x}_\perp)\frac{dI_0}{d\omega}. \qquad (24)$$

By comparing with Equation (20), we see that, in the limit $\delta p_z t \gg 1$, the echo intensity factor is $F(t,\vec{x}_\perp) = \mathcal{T}(t,\vec{x}_\perp)/t_{\text{sat}}$. This means that, when the echo saturation is predominantly due to one of the transverse average axion's velocity or velocity dispersion, the maximum value of $F$ tends to one for times larger than $t_{\text{sat}}$, provided $t_{\text{off}} > t_{\text{sat}}$.

Figure 1 shows the echo intensity factor at resonance, i.e., for $\bar{\omega} = (m + \langle p_z\rangle)/2$, for parameters compatible with the caustic ring model. We can clearly see the echo's "hot spot" spreading in the direction of the axion average velocity until the beam is turned off at $mt_{\text{off}} = 1.4 \times 10^9$. Thereafter, the hot spot stops spreading and starts traveling rigidly.

Figure 2 shows the echo intensity factor at resonance in a case of saturation due to velocity dispersion effects for parameters compatible with the isothermal sphere model. The hot spot spreads out in all directions, while at the same time, the maximum intensity grows until the beam is turned off. After that, the maximum intensity quickly drops to zero. Finally, we would like to comment on the echo profile in the frequency space. Figure 3 shows $F(t,\vec{0})$ as a function of the beam frequency $\omega$ at different times. The intensity factor was multiplied by the spectral intensity inherited from the beam $dI_0/d\omega|_{\omega=\Omega}$, whose maximum value was normalized to one. The beam spectral intensity, normalized to its maximum value, is shown in black. The echo peaks at a frequency $\bar{\Omega} = (m - \langle p_z\rangle)/2$, while the beam is centered at $\bar{\omega} = (m + \langle p_z\rangle)/2$. The echo bandwidth is given by $\delta\omega\delta p_z/(2\Delta)$. It is then possible for the echo frequency band to be completely separated from the beam frequency band if:

$$|\bar{\Omega} - \bar{\omega}| > \delta\omega + \frac{\delta\omega\delta p_z}{2\Delta}. \qquad (25)$$

Such a configuration may be advantageous to separate the signal from the noise if a part of the latter comes from the outgoing beam itself or from backscattering in the atmosphere.
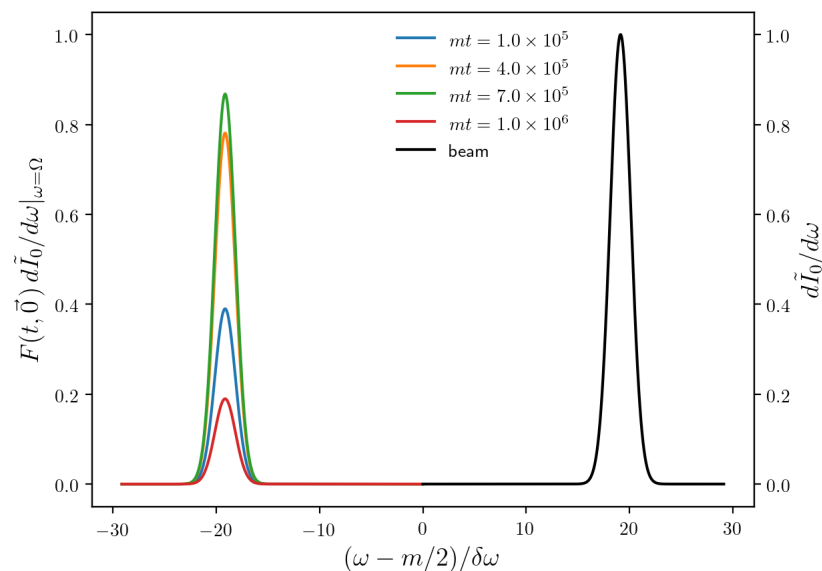


**Figure 3.** Frequency profile of the form factor times the spectral intensity $F(t,\vec{0})dI_0/d\omega|_{\omega=\Omega}$ (colored lines) and rescaled beam frequency profile $d\tilde{I}_0/d\omega$ (black line) at resonance $\omega = \omega_*$ in the isothermal halo model. All the parameters are the same as those of Figure 2, with the addition of $\delta\omega = 2 \times 10^{-5}$ m.

### 4. Echo Collected Power and Sensitivity

The power collected over a surface $S$ laying in the $z = 0$ plane can be computed as:

$$P_c = \frac{1}{16}\sqrt{\frac{\pi}{2}\frac{g^2\rho}{\Delta}}\, P_0\, \frac{1}{S_0}\int_S d^2x_\perp\, \mathcal{T}(t,\vec{x}_\perp), \tag{26}$$

where $S_0$ is the effective cross-sectional area of the beam at $z = 0$, $P_0 = I_0 S_0$ is the power of the beam, and:

$$\Delta = \sqrt{\delta\omega^2 + \frac{\delta p_z^2}{4}}. \tag{27}$$

We estimated the sensitivity of the echo method assuming that the echo power is collected by a dish antenna with radius $R_c$, located in the plane $z = 0$ and concentric with respect to the emitter. In this configuration, and for $R_c > R$, we have $\frac{1}{S_0}\int_S d^2x_\perp\, \mathcal{T}(t,\vec{x}_\perp) \approx \min(t, t_\perp)$, where $t_\perp$ is defined as:

$$t_\perp = R_c\left\langle v_\perp^{-1}\right\rangle. \tag{28}$$

The signal-to-noise ratio is given by Dick's radiometer equation:

$$s/n = \frac{P_c}{T_n}\sqrt{\frac{t_m}{B}}, \tag{29}$$

where $P_c$ is the collected power, $T_n$ the noise temperature, $B$ the bandwidth of the signal given roughly by $B \approx \min(\delta\omega, \delta p_z/2)/(2\pi)$, and $t_m$ the measurement time.

We determined $t_m$ as the time at which the power collected by the receiver drops off. The echo spreads all over the receiver in a time $t_\perp$. If at time $t_\perp$, the beam is still on, the collected power will drop at $t = t_{\text{off}}$. On the other hand, if the beam is turned off before $t_\perp$, the power collected will drop off then at $t = t_\perp$. In summary, the measurement time is given roughly by the maximum between $t_{\text{off}}$ and $t_\perp$.

The solid blue lines of Figure 4 mark the parameter space where the echo method is sensitive, assuming a fixed amount of energy $E = 10\,\text{MW y}$ is spent to cover an octave in axion mass. We assumed this energy is delivered with the largest power compatible with the constraint $t_{\text{off}} \geq (2\delta\omega)^{-1/2}$. This choice maximizes the sensitivity for a given bandwidth. However, in some parts of the parameter space, too large a power would be required. We also assumed $s/n = 5$, $T_n = 20\,\text{K}$, $R = 50\,\text{m}$, $R_c = 100\,\text{m}$ and $\delta\omega = \delta p_z/2$. For both the isothermal model (right panel) and the caustic ring model (left panel), we assumed minimal average axion transverse velocity: $v_p = 0$ and $v_p = 5\,\text{km/s}$, respectively. For the isothermal sphere model, we used a velocity dispersion $220\,\text{km/s}$. Figure 4 shows a range of axion masses compatible with the working frequency of radio telescopes.

The dashed blue lines of Figure 4 correspond to the sensitivities using a power source of $P_0 = 10\,\text{MW}$ working for 1 y. The other parameters are the same as for the solid blue lines. Despite the fact that the amount of energy spent is the same as for the solid lines, the sensitivity is worse. It is likely possible, though, to approach the solid lines' sensitivity by setting up the experiment in a clever way.
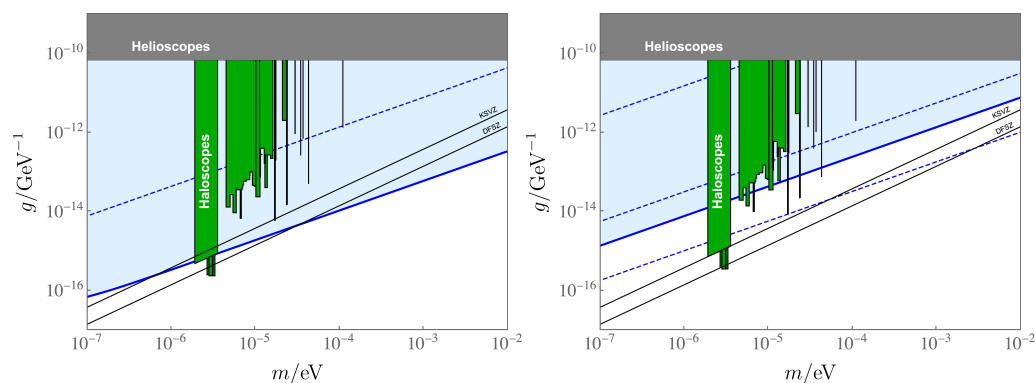
**Figure 4.** Expected sensitivity of the echo method in the space of parameters $(m, g)$ for the caustic ring (**left**) and isothermal model (**right**) of the galactic halo. These plots assume that the method consumes an energy of 10 MW y per a factor of two in the axion mass range. The difference between the solid and dashed lines is explained in the main text. The green regions are current bounds from axion dark matter haloscopes [31–44], and the grey region corresponds to bounds from the CAST experiment [45].

## 5. Conclusions

In this manuscript, we presented a description of the echo method for axion dark matter detection proposed in [21]. The echo intensity grows in time until it saturates after a characteristic time scale that depends on the transverse axion's velocity distribution. We classified this velocity distribution effect into two cases: small and large dispersion, depending on whether the transverse velocity dispersion is smaller or larger than the transverse average velocity. We also showed that it is possible to achieve a separation in frequency between the beam and echo bandwidths, thanks to the average velocity of the axion flow along the beam's direction relative to the lab frame. This may help reduce the noise from atmospheric backscattering and beam leakages.

We provided sensitivity estimates assuming a 100 m receiving dish and a power of 10 MW. These experimental parameters are attainable with currently available technology. For instance, the receiver could be a radio telescope such as the Green Bank and Effelsberg of FAST, while the power source could be a high-power klystron, as used for radar transmitters or particle accelerators.

Our sensitivity estimates agree with those of [21] when considering velocity distribution effects and also with the fact that the outgoing beam divergence does not play any role in the signal. The echo method appears an attractive approach to axion dark matter detection because it needs relatively old technology and because it is applicable over a wide range of axion masses.

## References

1. Boyarsky, A.; Drewes, M.; Lasserre, T.; Mertens, S.; Ruchayskiy, O. Sterile neutrino Dark Matter. *Prog. Part. Nucl. Phys.* **2019**, *104*, 1–45. [CrossRef]
2. Nelson, A.E.; Scholtz, J. Dark Light, Dark Matter and the Misalignment Mechanism. *Phys. Rev. D* **2011**, *84*, 103501. [CrossRef]
3. Peccei, R.; Quinn, H.R. CP Conservation in the Presence of Instantons. *Phys. Rev. Lett.* **1977**, *38*, 1440–1443. [CrossRef]
4. Weinberg, S. A New Light Boson? *Phys. Rev. Lett.* **1978**, *40*, 223–226. [CrossRef]
5. Wilczek, F. Problem of Strong *P* and *T* Invariance in the Presence of Instantons. *Phys. Rev. Lett.* **1978**, *40*, 279–282. [CrossRef]
6. Svrcek, P.; Witten, E. Axions In String Theory. *J. High Energy Phys.* **2006**, *06*, 051. [CrossRef]
7. Preskill, J.; Wise, M.B.; Wilczek, F. Cosmology of the Invisible Axion. *Phys. Lett. B* **1983**, *120*, 127–132. [CrossRef]
8. Abbott, L.; Sikivie, P. A Cosmological Bound on the Invisible Axion. *Phys. Lett. B* **1983**, *120*, 133–136. [CrossRef]
9. Dine, M.; Fischler, W. The Not So Harmless Axion. *Phys. Lett. B* **1983**, *120*, 137–141. [CrossRef]
10. Arias, P.; Cadamuro, D.; Goodsell, M.; Jaeckel, J.; Redondo, J.; Ringwald, A. WISPy Cold Dark Matter. *J. Cosmol. Astropart. Phys.* **2012**, *06*, 013. [CrossRef]
11. Sikivie, P. Invisible Axion Search Methods. *Rev. Mod. Phys.* **2021**, *93*, 015004. [CrossRef]
12. Irastorza, I.G.; Redondo, J. New experimental approaches in the search for axion-like particles. *Prog. Part. Nucl. Phys.* **2018**, *102*, 89–159. [CrossRef]
13. Sikivie, P. Experimental Tests of the Invisible Axion. *Phys. Rev. Lett.* **1983**, *51*, 1415–1417; Erratum in *Phys. Rev. Lett.* **1984**, *52*, 695. [CrossRef]
14. Hertzberg, M.P.; Schiappacasse, E.D. Dark Matter Axion Clump Resonance of Photons. *J. Cosmol. Astropart. Phys.* **2018**, *11*, 004. [CrossRef]
15. Caputo, A.; Garay, C.P.; Witte, S.J. Looking for Axion Dark Matter in Dwarf Spheroidals. *Phys. Rev. D* **2018**, *98*, 083024; Erratum in *Phys. Rev. D* **2019**, *99*, 089901. [CrossRef]
16. Arza, A. Photon enhancement in a homogeneous axion dark matter background. *Eur. Phys. J. C* **2019**, *79*, 250. [CrossRef]
17. Caputo, A.; Regis, M.; Taoso, M.; Witte, S.J. Detecting the Stimulated Decay of Axions at RadioFrequencies. *J. Cosmol. Astropart. Phys.* **2019**, *03*, 027. [CrossRef]
18. Wang, Z.; Shao, L.; Li, L.X. Resonant instability of axionic dark matter clumps. *J. Cosmol. Astropart. Phys.* **2020**, *07*, 038. [CrossRef]
19. Arza, A.; Schwetz, T.; Todarello, E. How to suppress exponential growth—On the parametric resonance of photons in an axion background. *J. Cosmol. Astropart. Phys.* **2020**, *10*, 013. [CrossRef]
20. Levkov, D.; Panin, A.; Tkachev, I. Radio-emission of axion stars. *Phys. Rev. D* **2020**, *102*, 023501. [CrossRef]
21. Arza, A.; Sikivie, P. Production and detection of an axion dark matter echo. *Phys. Rev. Lett.* **2019**, *123*, 131804. [CrossRef] [PubMed]
22. Arza, A.; Todarello, E. The axion dark matter echo: A detailed analysis. *arXiv* **2021**, arXiv:2108.00195.
23. Turner, M.S. Cosmic and Local Mass Density of Invisible Axions. *Phys. Rev. D* **1986**, *33*, 889–896. [CrossRef] [PubMed]
24. Duffy, L.; Sikivie, P. The Caustic Ring Model of the Milky Way Halo. *Phys. Rev. D* **2008**, *78*, 063508. [CrossRef]
25. Foster, J.W.; Rodd, N.L.; Safdi, B.R. Revealing the Dark Matter Halo with Axion Direct Detection. *Phys. Rev. D* **2018**, *97*, 123006. [CrossRef]
26. Hui, L.; Joyce, A.; Landry, M.J.; Li, X. Vortices and waves in light dark matter. *J. Cosmol. Astropart. Phys.* **2021**, *01*, 011. [CrossRef]
27. Centers, G.P.; Blanchard, J.W.; Conrad, J.; Figueroa, N.L.; Garcon, A.; Gramolin, A.V.; Kimball, D.F.; Lawson, M.; Pelssers, B.; Smiga, J.A.; et al. Stochastic fluctuations of bosonic dark matter. *arXiv* **2019**, arXiv:1905.13650.
28. Sikivie, P. Evidence for ring caustics in the Milky Way. *Phys. Lett. B* **2003**, *567*, 1–8. [CrossRef]
29. Banik, N.; Christopherson, A.J.; Sikivie, P.; Todarello, E.M. New astrophysical bounds on ultralight axionlike particles. *Phys. Rev. D* **2017**, *95*, 043542. [CrossRef]
30. Chakrabarty, S.S.; Han, Y.; Gonzalez, A.; Sikivie, P. Implications of triangular features in the Gaia skymap for the Caustic Ring Model of the Milky Way halo. *arXiv* **2020**, arXiv:2007.10509.
31. De Panfilis, S.; Melissinos, A.C.; Moskowitz, B.E.; Rogers, J.T.; Semertzidis, Y.K.; Wuensch, W.; Halama, H.J.; Prodell, A.G.; Fowler, W.B.; Nezrick, F.A. Limits on the Abundance and Coupling of Cosmic Axions at 4.5-Microev < m(a) < 5.0-Microev. *Phys. Rev. Lett.* **1987**, *59*, 839. [CrossRef]
32. Hagmann, C.; Sikivie, P.; Sullivan, N.S.; Tanner, D.B. Results from a search for cosmic axions. *Phys. Rev. D* **1990**, *42*, 1297–1300. [CrossRef] [PubMed]
33. Du, N.; Force, N.; Khatiwada, R.; Lentz, E.; Ottens, R.; Rosenberg, L.J.; Rybka, G.; Carosi, G.; Woollett, N.; Bowring, D.; et al. A Search for Invisible Axion Dark Matter with the Axion Dark Matter Experiment. *Phys. Rev. Lett.* **2018**, *120*, 151301. [CrossRef]
34. Braine, T.; Cervantes, R.; Crisosto, N.; Du, N.; Kimes, S.; Rosenberg, L.J.; Rybka, G.; Yang, J.; Bowring, D.; Chou, A.S.; et al. Extended Search for the Invisible Axion with the Axion Dark Matter Experiment. *Phys. Rev. Lett.* **2020**, *124*, 101303. [CrossRef]
35. Boutan, C.; Jones, M.; LaRoque, B.H.; Oblath, N.S.; Cervantes, R.; Du, N.; Force, N.; Kimes, S.; Ottens, R.; Rosenberg, L.J.; et al. Piezoelectrically Tuned Multimode Cavity Search for Axion Dark Matter. *Phys. Rev. Lett.* **2018**, *121*, 261302. [CrossRef]
36. Lee, S.; Ahn, S.; Choi, J.; Ko, B.R.; Semertzidis, Y.K. Axion Dark Matter Search around 6.7 μeV. *Phys. Rev. Lett.* **2020**, *124*, 101802. [CrossRef]
37. Jeong, J.; Youn, S.; Bae, S.; Kim, J.; Seong, T.; Kim, J.E.; Semertzidis, Y.K. Search for Invisible Axion Dark Matter with a Multiple-Cell Haloscope. *Phys. Rev. Lett.* **2020**, *125*, 221302. [CrossRef] [PubMed]

38. Kwon, O.; Lee, D.; Chung, W.; Ahn, D.; Byun, H.; Caspers, F.; Choi, H.; Choi, J.; Chung, Y.; Jeong, H.; et al. First Results from an Axion Haloscope at CAPP around 10.7 μeV. *Phys. Rev. Lett.* **2021**, *126*, 191802. [CrossRef]

39. Zhong, L.; Al Kenany, S.; Backes, K.M.; Brubaker, B.M.; Cahn, S.B.; Carosi, G.; Gurevich, Y.V.; Kindel, W.F.; Lamoreaux, S.K.; Lehnert, K.W.; et al. Results from phase 1 of the HAYSTAC microwave cavity axion experiment. *Phys. Rev. D* **2018**, *97*, 092001. [CrossRef]

40. Backes, K.M.; Palken, D.A.; Al Kenany, S.; Brubaker, B.M.; Cahn, S.B.; Droster, A.; Hilton, G.C.; Ghosh, S.; Jackson, H.; Lamoreaux, S.K.; et al. A quantum-enhanced search for dark matter axions. *Nature* **2021**, *590*, 238–242. [CrossRef]

41. Alesini, D.; Braggio, C.; Carugno, G.; Crescini, N.; D'Agostino, D.; Di Gioacchino, D.; Di Vora, R.; Falferi, P.; Gallo, S.; Gambardella, U.; et al. Galactic axions search with a superconducting resonant cavity. *Phys. Rev. D* **2019**, *99*, 101101. [CrossRef]

42. Alesini, D.; Braggio, C.; Carugno, G.; Crescini, N.; D'Agostino, D.; Di Gioacchino, D.; Di Vora, R.; Falferi, P.; Gambardella, U.; Gatti, C.; et al. Search for invisible axion dark matter of mass $m_a = 43$ μeV with the QUAX–$a\gamma$ experiment. *Phys. Rev. D* **2021**, *103*, 102004. [CrossRef]

43. McAllister, B.T.; Flower, G.; Ivanov, E.N.; Goryachev, M.; Bourhill, J.; Tobar, M.E. The ORGAN Experiment: An axion haloscope above 15 GHz. *Phys. Dark Univ.* **2017**, *18*, 67–72. [CrossRef]

44. Melcón, A.Á; Cuendis, S.A.; Baier, J.; Barth, K.; Bräuniger, H.; Calatroni, S.; Cantatore, G.; Caspers, F.; Castel, J.F.; Cetin, S.A.; et al. First results of the CAST-RADES haloscope search for axions at 34.67 μeV. *arXiv* **2021**, arXiv:2104.13798.

45. Anastassopoulos, V.; Aune, S.; Barth, K.; Belov, A.; Cantatore, G.; Carmona, J.M.; Castel, J.F.; Cetin, S.A.; Christensen, F.; Collar, J.I.; et al. New CAST Limit on the Axion-Photon Interaction. *Nat. Phys.* **2017**, *13*, 584–590. [CrossRef]